Electronic Supplementary Material (ESI) for Journal of Materials Chemistry C.


# Supporting Information

## Electron-deficient multicenter bonding in pnictogens and chalcogens: mechanism of formation

Hussien H. Osman[1,2,3*], Alberto Otero-de-la-Roza[4], P. Rodríguez-Hernández[5], Alfonso Muñoz[5], and Francisco J. Manjón[1*]

[1] Instituto de Diseño para la Fabricación y Producción Automatizada, MALTA Consolider Team, Universitat Politècnica de València, 46022, València, Spain.

[2] Instituto de Ciencia de los Materiales de la Universitat de València, MALTA Consolider Team, Universitat de València, 46100, Burjassot, Valencia, Spain.

[3] Chemistry Department, Faculty of Science, Helwan University, Ain-Helwan, 11795, Cairo, Egypt.

[4] Departamento de Química Física y Analítica, MALTA Consolider Team, Universidad de Oviedo, 33006, Oviedo, Spain.

[5] Departamento de Física, Instituto de Materiales y Nanotecnología, MALTA Consolider Team, Universidad de La Laguna, 38205, La Laguna, Tenerife, Spain.

*Corresponding author(s). E-mail(s): hussien.helmy@uv.es; fjmanjon@fis.upv.es

## 1. Computational details.

First-principles calculations were performed using the density-functional theory (DFT) as implemented in the Vienna Ab initio Simulation Package (VASP) code [1–3]. All calculations were implemented at the generalized gradient approximation (GGA) level, using the Perdew–Burke–Ernzerhof (PBE) exchange-correlation functional [4] with the projector augmented-wave (PAW) method [5]. The PBE functional revised for solids (PBEsol) [6] has provided improved structural parameters that reasonably agree with experimental results for the As-I, Sb-I, Bi-I, Bi-II, Se-I, and Te-I phases. Additional calculations for the Bi-I phase were performed using the AM05 functional [7–9]. Semi-core d electrons were included for As, Bi, and Po elements. Spin-orbital coupling (SOC) was included for the heavy elements Bi and Po. Brillouin-zone integrals were approximated using Γ-centered Monkhorst–Pack meshes [10]. Dense *k*-point grids of 15 × 15 × 15 were applied for the rhombohedral or trigonal crystals, 9 × 9 × 9 for the cubic crystals, and 7 × 7 × 11 for the monoclinic Bi-II structure. The wavefunction was expanded in plane waves up to a cut-off energy of 500 eV for As, Bi, and Po and 300 eV for Sb, Se, and Te to ensure convergence of the total energy within $10^{-5}$ eV per atom. Under the selected pressure range, lattice parameters and atomic positions were fully optimized using the conjugate-gradient method until the forces on atoms were smaller than $10^{-4}$ eV $Å^{-1}$. Further information about the lattice parameters and bond distances at ambient conditions is tabulated in **Tables S1** and **S2**.

Density-functional perturbation theory (DFPT) was used to calculate phonon frequencies (ω) as well as the Born effective charge (BEC, Z*) tensor of the constituent atoms. Phonon-dispersion curves of the A7 phase of Bi at 10 GPa were computed by using the supercell finite-displacement method implemented in the Phonopy package [11] with VASP as the force constant calculator. A 2 × 2 × 2 supercell was used to enable the exact calculation of frequencies at the zone center (Γ) and unique zone-boundary wave vectors. The phonon-dispersion curves were obtained on uniform 40 × 40 × 40 Γ-centered *q*-point meshes. Our lattice dynamics calculations do not include long-range interaction of the electric field, so only transversal optical phonons are obtained in all simulated phases. Further information about the bonding characteristics was extracted from the calculated electron localization function (ELF) for selected elements. Optimized crystal structures and related data were visualized by VESTA program [12]. The calculated volumetric data was fitted to the third-order Birch-Murnaghan equation of state (BM3-EOS) using the EosFit7 software [13].

Delocalization index (DI) calculations, used to calculate the number of electrons shared, ES = 2 × DI, were carried out using a Wannier transformation as detailed in Ref. [14]. For this purpose, Quantum ESPRESSO, version 6.5 [15], was used in combination with wannier90 [16] and the CRITIC2 program [17]. Single-point calculations at the VASP equilibrium geometries were

carried out using the same uniform k-point grids as in VASP, a plane-wave cutoff of 80 Ry and a density cutoff of 320 Ry. Both the norm-conserving pseudopotentials (for the Kohn-Sham states) and the PAW [5] data sets (for the all-electron density) were obtained from the pslibrary [18]. The PBEsol functional was used for the DI calculations [6]. Further chemical-bonding analysis was performed through the crystal-orbital bond index (COBI) and projected crystal-orbital Hamilton population (pCOHP) plots generated by the LOBSTER program [19–22]. These calculations use the initial wavefunction and full electronic density calculated by VASP.

## 2. Crystal structures of pnictogens and chalcogens.

At room pressure (RP), the As-I, Sb-I, and Bi-I phases of group-15 elements have a trigonal A7 crystal structure (space group *R*-3*m*, *No.* 166) [23]. The primitive unit cell has two atoms characterized by the Wyckoff position *6c* (0 0 *u*), where *u* is the internal position parameter. The A7 phase shows a layered structure in which each atom is surrounded by the three nearest atoms (intralayer) and three second nearest (interlayer) neighbors at $d_1$ and $d_2$ bond distances, respectively. More details regarding the experimental and calculated cell parameters, intralayer ($d_1$), and interlayer ($d_2$) distances of the A7 structure in crystalline group-15 elements at RP are collected in **Table S1**. In particular, **Table S1** shows that $d_1$ and $d_2$ distances become close to each other as the sixfold coordination is approached going from As to Bi. The shorter $d_2/d_1$ ratio in Bi implies a stronger interlayer bonding than in As and Sb.

The three group-15 elements show experimental phase transitions (PTs) at high pressure (HP) in which the transition pressure ($P_t$) decreases going down the group. The A7-to-$A_h$ PT has been observed at 25 GPa in As [24]. Sb-I transforms to a monoclinic incommensurate host-guest Sb-IV phase at 8.0 GPa. This phase transforms at 8.6 GPa to a tetragonal incommensurate host-guest Sb-II [25–27]. The later phase transforms to the body-centered cubic (*bcc*) Sb-III phase at 28 GPa [28]. The $A_h$ phase has been proposed to exist in Sb either at HP [29], or at RP [30], but recent studies have not confirmed previous results [31]. On the other hand, the $A_h$ phase does not exist among the HP phases of Bi [32]. At 2.52 GPa, Bi-I transforms to monoclinic Bi-II with a narrow stability pressure range [33–36]. A Bi-III phase with host-guest structure is found between 2.7 and 7.7 GPa [32,37,38]. At higher pressures, the Bi-V phase, with *bcc* structure, is observed and found stable up to 220 GPa [39,40].

At RP, the Se-I and Te-I phases of group-16 elements crystallize in the trigonal A8 crystal structure (space group $P3_121$, No. 152). The unit cell has three atoms at the positions (*u* 0 0), (0 *u* 1/3), and ($\bar{u}$ $\bar{u}$ 2/3), where *u* is the internal atomic position parameter. This structure has infinite twofold coordinated helical chains running along the *c*-axis, where each atom is connected to two nearest atoms by strong covalent intrachain bonds at $d_1$ distance and to four second-nearest atoms by relatively weak interchain bonds at $d_2$ distance. Information about the cell parameters and the

intrachain ($d_1$) and interchain ($d_2$) distances in the A8 phase of group-16 crystalline elements at different pressures can be found in **Table S2**. In particular, **Table S2** shows that $d_1$ and $d_2$ distances become close to each other as the sixfold coordination is approached on going from Se to Te. The large $d_2/d_1$ ratio in Se indicates a weaker interchain bonding than in Te. The bonding in Se is nearly similar to that of an ideal molecular crystal since its covalent radius ($R_c$) is 1.20 Å [41] which results in 2 $R_c \approx$ d1. In Te, $R_c$ is 1.38 Å [41] resulting in $2R_c < d_1$. Consequently, the intralayer bond $d_1$ in Te is weaker than the intralayer bond $d_1$ in Se.

At HP, Se-I transforms to the C-face-centered monoclinic host-guest structure (Se-II) at 16-18 GPa and then to a different base-centered monoclinic Se-III phase at 23 GPa. Se-III transforms to an incommensurately modulated monoclinic structure (Se-IV) at 28 GPa, which is followed by a transition to a β-Po-type rhombohedral phase (Se-V) at 41 GPa [42,43]. On the other hand, Te-I transforms to the triclinic Te-II phase at 4 GPa. The Te-II phase transforms to an incommensurately modulated monoclinic structure (Te-III) at 7 GPa. The Te-III phase goes to the rhombohedral β-Po-type phase (Te-IV) above 10 GPa, but this result is contradictory [44]. Finally, a transition to a *bcc* phase (Te-V) occurs at 27 GPa [45–49].

Polonium has two polymorphs at RP. The low-temperature polymorph, α-Po, and the high-temperature polymorph, β-Po. α-Po crystallizes in the $A_h$ phase (simple cubic (*sc*), space group *Pm*-3*m*, *No*. 221), whereas β-Po crystallizes in the $A_i$ phase (rhombohedral space group *R*-3*m, No*. 166). In α-Po, there is a single Po atom at a *1a* site, and the only free parameter is the lattice parameter of the simple cubic lattice. In β-Po, there is a single atom at a *3a* site and there are two free parameters, the rhombohedral lattice parameter and the rhombohedral angle of the rhombohedral unit cell (or alternatively the *a* and *c* lattice parameters of the hexagonal unit cell). Both polymorphs of Po show an octahedral coordination, with a single bond distance, and the atomic packing is very similar to Se, Te, and the group-15 elements As, Sb, and Bi; however, the presence of lone electron pairs (LEPs) in these last elements at RP results in a high octahedral distortion [50]. From the chemical point of view, it is expected that Po is hexavalent since there are six electrons in the outer shell ($6s^2\ 6p^4$), but instead, it is tetravalent. The explanation of such anomalous behavior is the very high *sp* excitation energy in heavy atoms affecting the two electrons of *s*-type orbital that act as an inert LEP, like in thallium and lead [51]. The structural relation between group-16 elements, Se, Te, and Po, was previously discussed in detail [50,52].

**Table S1.** Calculated and experimental structural parameters of the A7 phase in group-15 elements at RP: cell parameters (in Å), $u$ parameter, intralayer, $d_1$, and interlayer, $d_2$, distances (in Å), and the $d_2/d_1$ ratio.

| Species | $a$ | $c/a$ | $u$ | $d_1$ | $d_2$ | $d_2/d_1$ |
|---|---|---|---|---|---|---|
| **As (A7, 0 GPa)** | 3.784 | 2.672 | 0.230 | 2.533 | 3.020 | 1.192 |
| **Expt. (0 GPa)** [53] | 3.759 | 2.805 | 0.227 | 2.516 | 3.121 | 1.240 |
| **As (A7, 30 GPa)** | 3.555 | 2.429 | 0.5 | 2.507 | 2.507 | 1.00 |
| **As ($A_h$, 30 GPa)** | 3.541 | 2.449 | | 2.504 | | |
| **Sb (A7, 0 GPa)** | 4.325 | 2.622 | 0.233 | 2.927 | 3.298 | 1.127 |
| **Expt. (0 GPa)** [54] | 4.308 | 2.617 | 0.233 | 2.908 | 3.355 | 1.154 |
| **Sb (A7, 10 GPa)** | 4.170 | 2.434 | 0.5 | 2.942 | 2.942 | 1.00 |
| **Sb ($A_h$, 10 GPa)** | 2.948 | | | 2.948 | | |
| **Expt. (7 GPa)** [29] | 2.896 | | | 2.896 | | |
| **Bi (A7, 0 GPa)** | 4.526 | 2.573 | 0.237 | 3.079 | 3.449 | 1.120 |
| **Expt. (0 GPa)** [55] | 4.546 | 2.602 | 0.234 | 3.071 | 3.529 | 1.149 |

**Table S2.** Calculated and experimental structural parameters of the A8 phase in group-16 elements at RP: cell parameter (in Å), intrachain, $d_1$, and interchain, $d_2$, distances (in Å), and the $d_2/d_1$ ratio in Se and Te. Structural data of the high-pressure $A_i$ phase in Se and Te together with α- and β-Po phases at RP are also provided.

| Species | $a$ | $c/a$ | $d_1$ | $d_2$ | $d_2/d_1$ |
|---|---|---|---|---|---|
| **Se (A8, 0 GPa)** | 4.028 | 1.275 | 2.444 | 3.165 | 1.295 |
| **Expt. (0 GPa)** [42] | 4.366 | 1.135 | 2.373 | 3.436 | 1.448 |
| **Se ($A_i$, 30 GPa)** | 3.257 | 1.657 | 2.602 | 2.602 | 1.00 |
| **Te (A8, 0 GPa)** | 4.377 | 1.361 | 2.917 | 3.335 | 1.143 |
| **Expt. (0 GPa)** [56] | 4.457 | 1.330 | 2.835 | 3.495 | 1.233 |
| **Te ($A_i$, 10 GPa)** | 3.762 | 1.687 | 3.032 | 3.032 | 1.00 |
| **α-Po** | 3.349 | | 3.349 | | |
| **Expt. (0 GPa)** [50] | 3.359 | | 3.359 | | |
| **β-Po** | 4.730 | 1.232 | 3.352 | | |
| **Expt. (0 GPa)** [50] | 4.486 | 1.399 | 3.368 | | |

## 3. Results on pnictogens.

The first step of our calculations is to study the effect of pressure on the stability of the known phases of group-15 and -16 elements at RP. The formation enthalpy difference (ΔH) of the As-I (A7) and As-II ($A_h$) phases at different pressures were calculated to evaluate the $P_t$ as shown in the inset of **Fig. S1a**. The $P_t$ is obtained at about 25 GPa, which is in good agreement with the experimental value. Both calculated and experimental atomic volumes of As vs. pressure are shown in **Fig. S1**. The BM3-EOS was employed to fit theoretical results to evaluate the bulk modulus ($B_0$) and its pressure derivative ($B_0$`) at zero pressure. Our results show good agreement with the experimental ones. In particular, the calculated relative volume ($V/V_0$) of the A7 phase at $P_t$ is 0.773, which is in reasonable agreement with previously reported experimental and calculated values of 0.772 and 0.8, respectively [24,57]. Moreover, the calculated bulk modulus (55.9 GPa) agrees reasonably with the experimental values previously reported (58 [24], 59 [58], and 55.6 GPa [59]). These values are in very good agreement if we consider that experimental (4.4 [59]) and calculated (4.1) $B_0$ values are comparable.

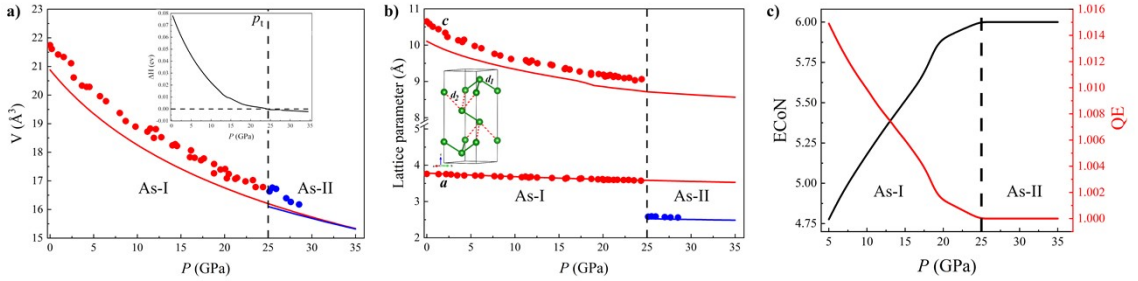


**Figure S1.** Calculated (line) and experimental (circle) structural parameters of the optimized A7 (red) and $A_h$ (blue) structures of elemental As as a function of hydrostatic pressure. a) Atomic volume fitted to the BM3-EOS. ΔH (relative to the A7 phase) is shown in the inset. b) Lattice parameters and an attached inset of the crystal lattice. c) Effective coordination number (ECoN) (black) of As and quadratic elongation (QE) (red) of As distorted octahedron in the A7 phase. The transition pressure, $P_t$, is marked with a vertical dashed line in all panels. Experimental data was obtained from Ref. [24].

The good agreement between the experimental and theoretical lattice parameters in As-I and As-II is shown in **Fig. S1b**. Clearly, the A7 structure shows an anisotropic compression in which the c-axis (related to interlayer distances) compresses much easier than the *a*-axis (related only to intralayer distances). At $P_t$, the lattice parameters are $a$ = 3.584 Å and $c$ = 8.714 Å for the A7 phase and 2.525 Å for the $A_h$ phase.

The effective coordination number (ECoN) can reflect the increase of atomic coordination when electron-deficient (metavalent) multicenter bonds (EDMBs) form. This was extensively discussed for various groups of materials including covalent, metallic, ionic, and metavalent materials in previous work (see **Fig. 2** in Ref. [60]). **Fig. S1c** shows the ECoN of the As atom in the A7 structure which is determined by examining As polyhedra at different pressures, adjusting the As-As distance to 3.0 Å. It is known that for normal covalent solids, the coordination number is low and obeys the $8 - N$ rule, e.g. As, Sb, and Bi are elements of group-15 that have an ECoN of 3 due to the three intralayer covalent bonds at RP. As pressure increases, the ECoN of the As atom increases gradually up to 25 GPa where the As atom is coordinated to ~ 6 neighbors, thus violating the $8 - N$ rule. These anomalous ECoN values are intermediate between that of pure covalent and pure metallic materials (see Fig. 2 in Ref. [60]). This provides evidence of the tendency of the As atoms to form EDMBs at HP. On the other hand, the quadratic elongation (QE) index, which measures the distortion in the coordination polyhedra, is also shown for As in **Fig. S1c**. The QE is inversely proportional to the ECoN and it decreases till it reaches ~ 1 at 25 GPa, where a nearly full octahedral coordination is obtained.

Following the same strategy as with elemental As, we have simulated the effect of pressure on the A7 phases of Sb (Sb-I) and Bi (Bi-I) (see **Fig. S2 and S4** in ESI). As already mentioned, the A7 phases of Sb and Bi also tend to transform into the $A_h$ phase. Interestingly, this phase has not been observed in Bi at HP, although the monoclinic Bi-II phase is a slightly distorted *sc* phase, and it remains uncertain whether it exists or not in Sb (see discussion in section 2 of ESI). In any case, we have calculated the A7-to-$A_h$ PT in both elements because it provides valuable insight into the decrease of the polyhedral distortion with respect to the octahedral coordination and to clarify the various stages of the pre-EDMB to EDMB transformation to be discussed in the next section.

Regarding Sb and Bi, the simulated atomic volume, lattice parameters, and phonon frequencies of Sb-I and Bi-I as a function of pressure (**Figs. S2 and S4** in ESI) show in general better agreement with the experiment than for As-I. These results suggest that anharmonic effects are less pronounced in Sb and Bi than in As although these elements at RP show bonds that are closer to the EDMBs than in As, as we will discuss later. Again, the presence of EDMBs in the $A_h$ phase in Sb and Bi is confirmed by the change in the sign of the simulated pressure coefficients of the optical phonon frequencies at $P_t$, the high value of $|\gamma_i|$ near $P_t$, the increase of the Z* value in the A7 phase and its high value in the octahedrally-coordinated $A_h$ phase, and by the negligible $\nabla^2\rho$ value in the $A_h$ phase. Therefore, despite that the $A_h$ phase could not be experimentally observed in these compounds at HP, it can be concluded that both Sb and Bi tend to exhibit EDMBs as pressure increases and octahedral coordination is approached.

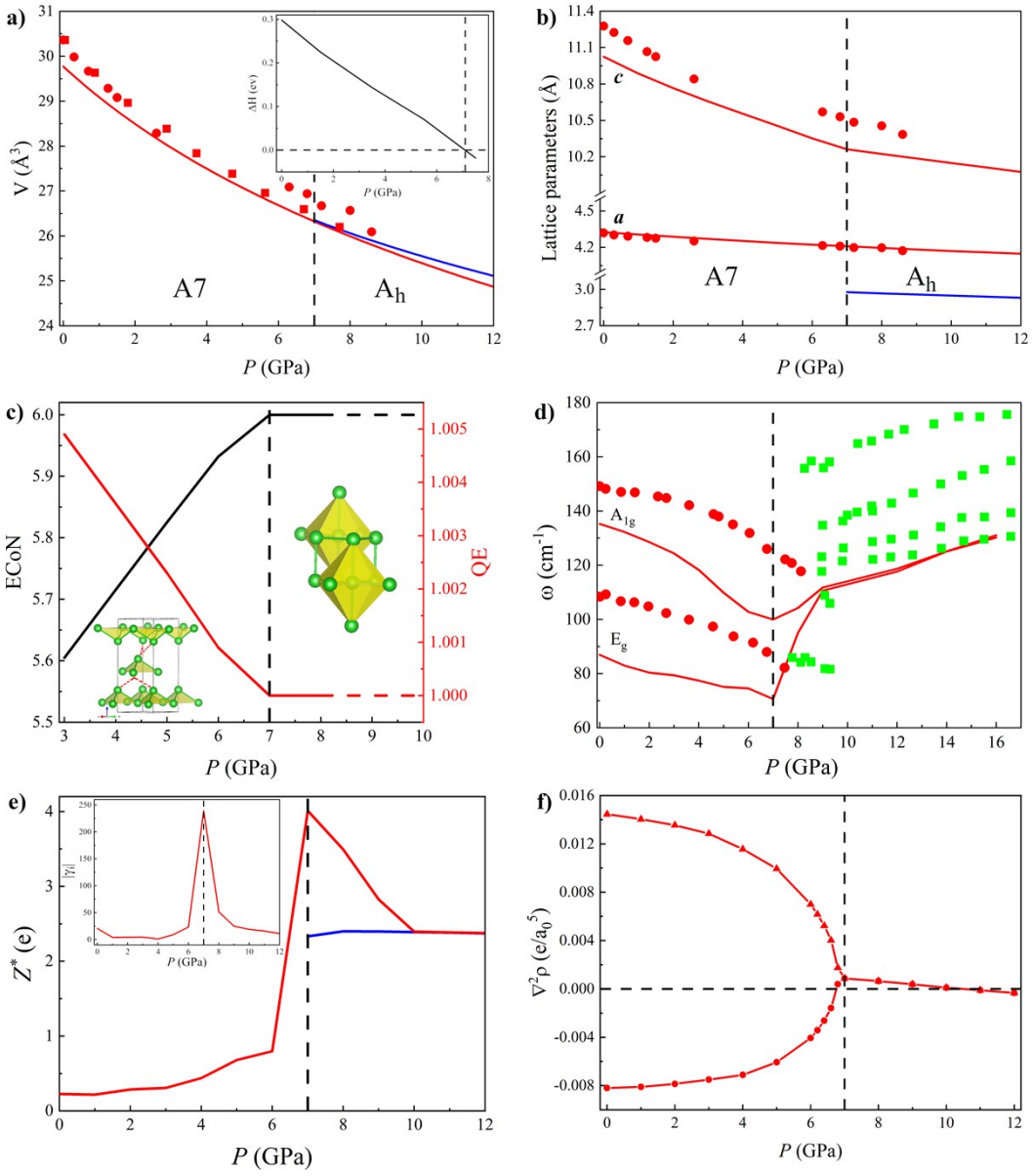


**Figure S2.** Calculated (line) and experimental (symbol) structural parameters of the optimized A7 (red) and $A_h$ (blue) structures of elemental Sb versus pressure. a) Atomic volume fitted to the BM3-EOS. Experimental data were obtained from Ref. [61] (circle) and Ref. [27] (square). ΔH (relative to A7 phase) is shown in the inset. b) Lattice parameters. The experimental data was obtained from Ref. [61]. c) Effective coordination number (ECoN) (black) of Sb and quadratic elongation (QE) (red) of the Sb polyhedron in the A7 phase. The attached insets show the Sb polyhedra in the A7 and $A_h$ phases. d) Phonon frequencies, ω: the two Raman-active $A_{1g}$ and $E_g$ modes of Sb-I. Experimental values for the Sb-I (circles) and Sb-II (squares) phases are obtained from Ref. [62]. e) Calculated average Born effective charge, Z*, tensor. Attached inset of the absolute Grüneisen parameter for the $A_{1g}$ mode. f) Laplacian of the charge density, where e is the electron charge and $a_0$ is the Bohr radius, at the BCP of primary (circle) and secondary (triangle) bonds of A7 and the only bond of $A_h$ structure. The transition pressure (Pt) is marked with a vertical dashed line in all panels.

Regarding Sb and Bi, our simulations also confirm the presence of the three stages of the mechanism of EDMB formation along the A7-to-$A_h$ PT (**Fig. S3, S5, and S12b-c** in ESI). In particular, Sb-I is in stage 1 at 0 GPa and in stage 2 above 3.5 GPa, whereas stage 3 should occur

experimentally in Sb-II above 8 GPa. On the other hand, Bi-I is in stage 1 (close to stage 2) at 0 GPa and in stage 2 (close to stage 3) in Bi-II at 2.5 GPa. Since the $A_h$ phase has not been experimentally reported in Bi, stage 3 should occur experimentally in Bi-III above 2.7 GPa, as already pointed out in the previous section. Interestingly, our results obtained for Bi are consistent with the comments of Häussermann et al. [136], who stated that the electronic band structure of Bi-III shows a Fermi level located in a valley in the bands formed by bonding and antibonding *p*-type orbitals with a "*significant covalent bonding contribution"*. They also noted that the "*covalent bonding contribution*" in Bi-III is no longer present in the A2 phase of group-15 elements that occurs at higher pressures, where a full electron delocalization is found, as expected in metallic bonding. In this context, we consider that the term "*significant covalent bonding contribution"* should be now understood as the EDMB contribution in Bi-III because EDMBs are also directional, like covalent bonds, and unlike metallic bonds. Finally, we have to stress that a progressive decrease of the pressure range of stages 1 and 2 is observed on going from As (stage 1: 0 - 15 GPa; stage 2: 15 - 25 GPa) to Sb (stage 1: 0 - 3.5 GPa; stage 2: 3.5 - 7 GPa) and Bi (stage 1: 0 - 2.5 GPa; stage 2: 2.5 - 2.7 GPa).

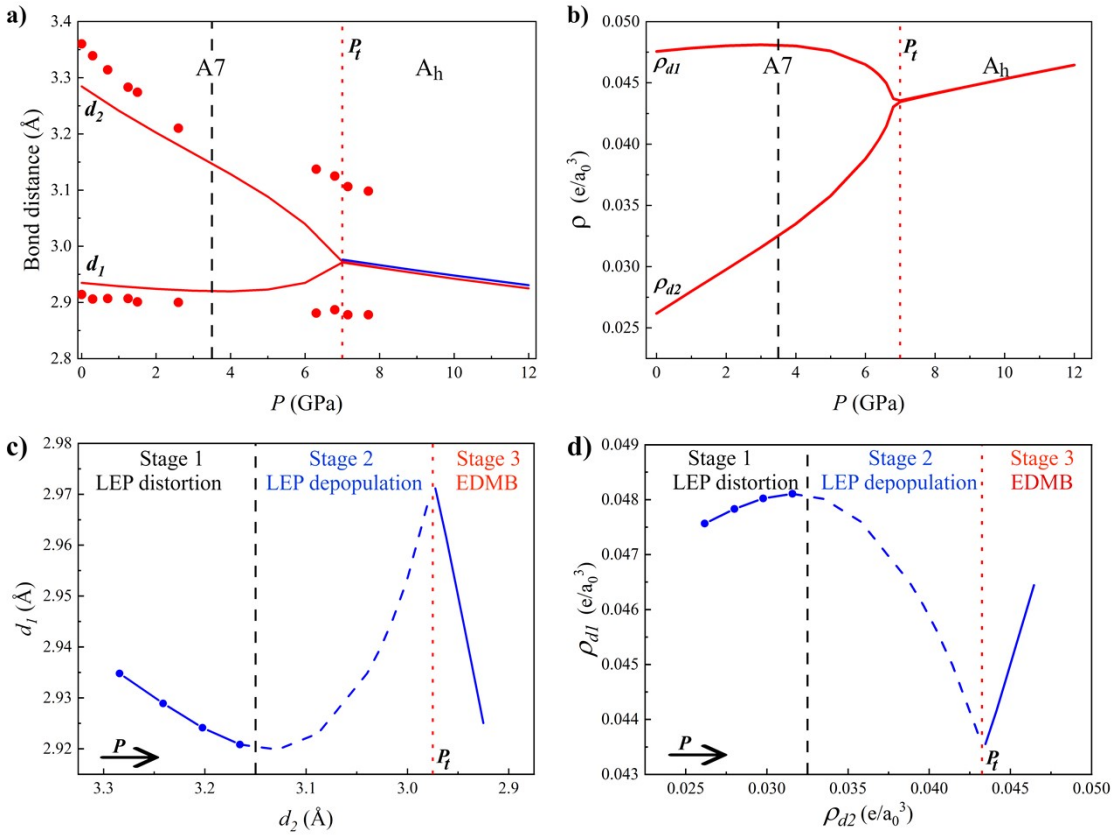


**Figure S3**. Calculated parameters of Sb as a function of pressure. a) Primary and secondary bond distances, $d_1$ and $d_2$, in the A7 (red) phase and the only bond distance of the $A_h$ (blue) phase. Experimental data was obtained from Ref. [61]. b) Charge density at the BCP of $d_1$ and $d_2$, $\rho_{d1}$ and $\rho_{d2}$, where $e$ is the electron charge and $a_0$ is the Bohr radius. c) Evolution of $d_1$ vs. $d_2$ and d) the corresponding $\rho_{d1}$ and $\rho_{d2}$. The three stages of the mechanism of EDMB formation (LEP distortion, LEP depopulation, and EDMB formation/LEP delocalization) are separated by vertical black dashed and red dotted lines.

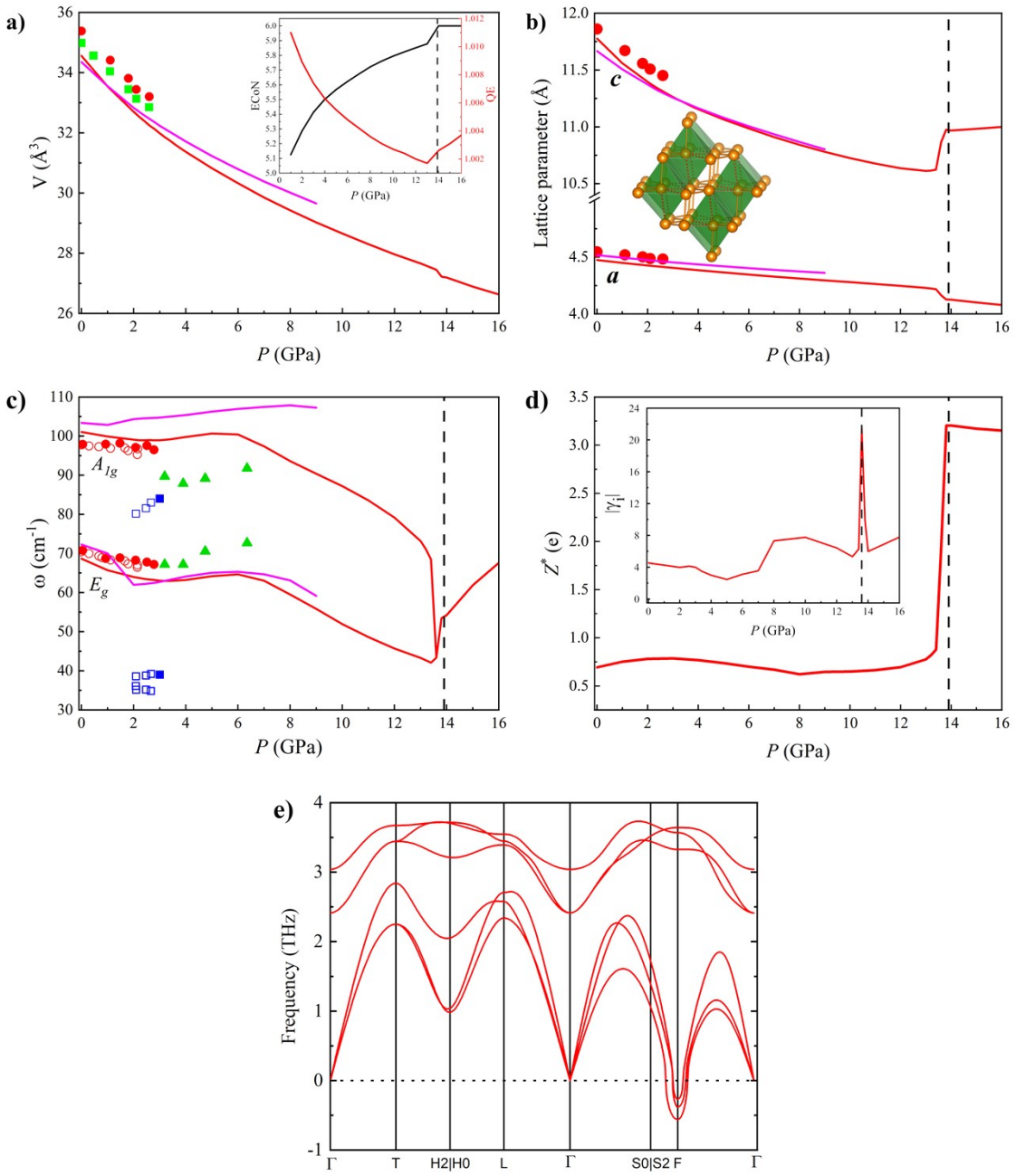


**Figure S4.** Calculated (line) and experimental (symbols) structural parameters of the optimized A7 structure of Bi (Bi-I) under pressure. Calculations were performed by using PBEsol (red) and AM05 (pink) functional. a) Atomic volume fitted to the BM3-EOS. Attached inset of the pressure dependence of the ECoN (black) and QE (red). b) Evolution of lattice parameters of the A7 phase. Attached inset of the Bi octahedral polyhedra. Experimental structural data is obtained from Ref. [26] (circle) and Ref. [38] (square). c) Phonon frequencies, ω: the two Raman-active $A_{1g}$ and $E_g$ modes for Bi-I (line) and experimental data points for Bi-I (circle), Bi-II (square), and Bi-III (triangle) were obtained from Ref. [63] (solid symbols) and Ref. [64] (open symbols). d) Calculated average Born effective charge, Z*, tensor and attached inset of absolute Grüneisen parameter. Vertical dashed lines represent the $P_t$. e) Phonon-dispersion curves of Bi-I at 10 GPa using the PBEsol functional.

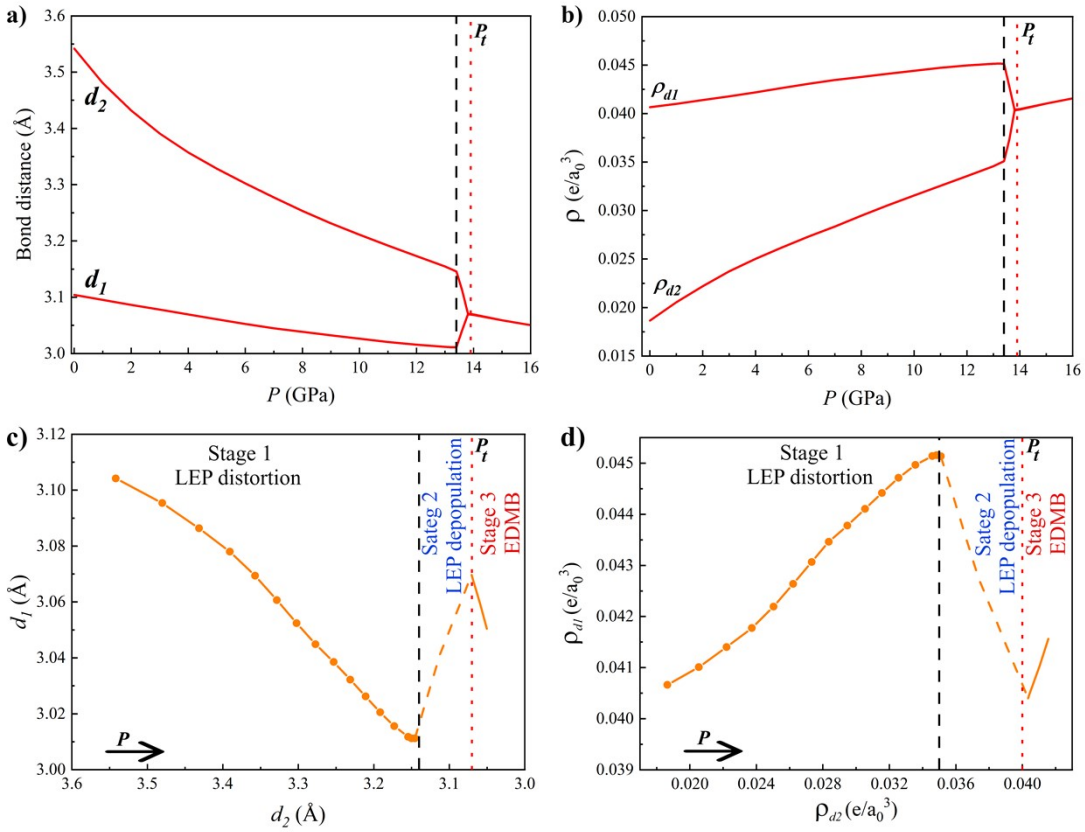


**Figure S5.** Calculated parameters of Bi-I as a function of pressure. (a) Primary and secondary bond distances, $d_1$ and $d_2$. b) Charge density at the BCP of $d_1$ and $d_2$, $\rho_{d1}$ and $\rho_{d2}$, where $e$ is the electron charge and $a_0$ is the Bohr radius. c) Evolution of $d_1$ vs. $d_2$ and d) the corresponding $\rho_{d1}$ and $\rho_{d2}$ along the three stages of the mechanism of EDMB formation. Vertical black dashed and red dotted lines separate the three stages of the mechanism.

Since the PBEsol functional works well for Bi below 6 GPa, we have simulated the monoclinic phase of Bi-II to check the occurrence of EDMBs in one of the HP phases of Bi. Bi-II has a distorted *sc* structure with a very narrow stability pressure range between 2.5 and 2.7 GPa. It undergoes a PT to the incommensurately modulated host-guest Bi-III structure above 2.7 GPa (Bi-III is isostructural to Sb-II, the HP phase of Sb above 9 GPa [117]). Our results for the optical phonons of Bi-II at HP (see **Fig. S6** in ESI) show a rather good agreement with experimental results [114,118] and a positive pressure coefficient for all the optical modes, as expected once EDMBs are formed. As expected, the calculated Z* value in Bi-II is much higher than that expected for a material with covalent or metallic bonds. Therefore, we conclude that the slightly distorted *sc* phase of Bi-II likely shows slightly asymmetric EDMBs.

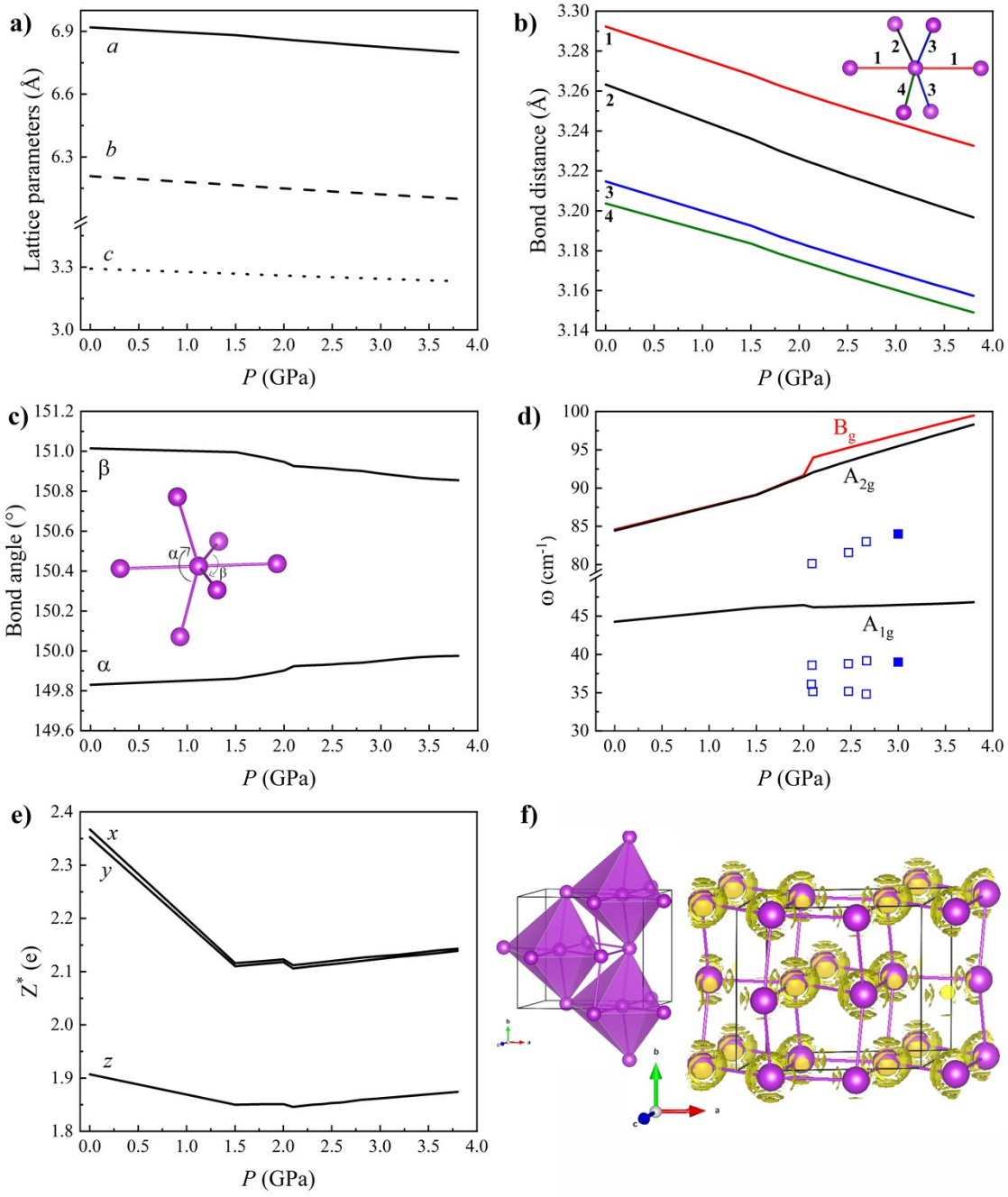


**Figure S6.** Calculated (PBEsol) physical parameters of the optimized monoclinic Bi structure (Bi-II phase) under pressure. a) Lattice parameters. b) Bond distances and an inset of the $Bi_6$ unit showing the different bonds. c) α and β angles between the bonds of a $Bi_6$ motif. d) Calculated phonon frequencies, ω, with experimental data obtained from Ref. [62] (solid square) and Ref. [64] (open square). e) The diagonal components of the Z* tensor. f) 3D ELF isosurface of value 0.565 and an inset of the Bi polyhedra in Bi-II.

## 4. Results on chalcogens.

**Figure S7a** illustrates the change in the atomic volume of Se-I as pressure is applied. The ΔH of the A8 and $A_i$ phases at different pressures were calculated to evaluate the $P_t$ as shown in the inset of **Fig. S7a**. The $P_t$ was obtained at 24 GPa. The lattice parameters of Se-I as a function of pressure are depicted in **Fig. S7b**. It is evident that the compression of Se-I is anisotropic, the *c*-axis increases smoothly while the a-axis gradually decreases with increasing pressure. The *a*-axis is the preferred direction for compression, as it allows the Se chains to approach each other, facilitating the formation of new bonds with neighbor Se atoms. ECoN and QE index are shown in **Fig. S7c**, with the Se-Se distance set to a maximum of 3.2 Å. The ECoN changes from two at 0 GPa to six at 24 GPa, corresponding to nearly sixfold coordination. Previous experimental results indicate that the XRD patterns at pressures above 18 GPa are very similar, with minor changes, suggesting that Se-II and Se-III are closely related structures (see Fig. 4 in Ref. [65]). The calculated pressure dependence of the bond distances and charge densities at the BCPs in A8 and $A_i$ phases of Se are plotted in **Fig. S8**.

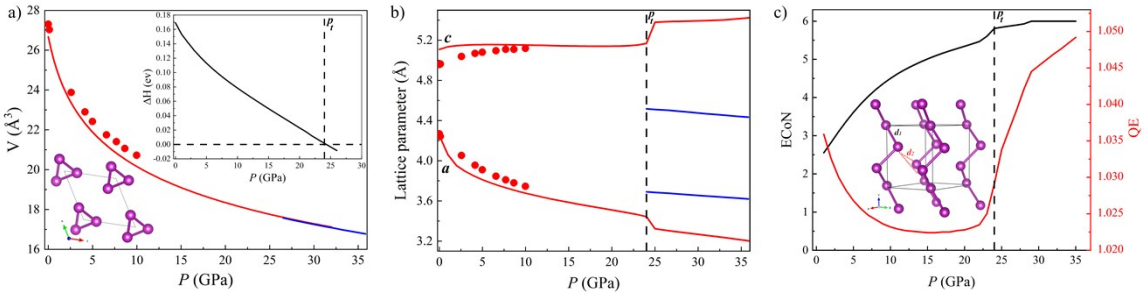


**Figure S7.** Calculated (line) and experimental (circle) structural parameters of Se under pressure in A8 (red) and $A_i$ (blue) phases. a) Atomic volume fitted to the BM3-EOS. The attached inset shows the ΔH (relative to the $A_i$ phase) and the crystal lattice viewed along the *c*-axis. b) Lattice parameters. c) The ECoN (black) and QE (red). $P_t$ is marked with a vertical dashed line in all panels.

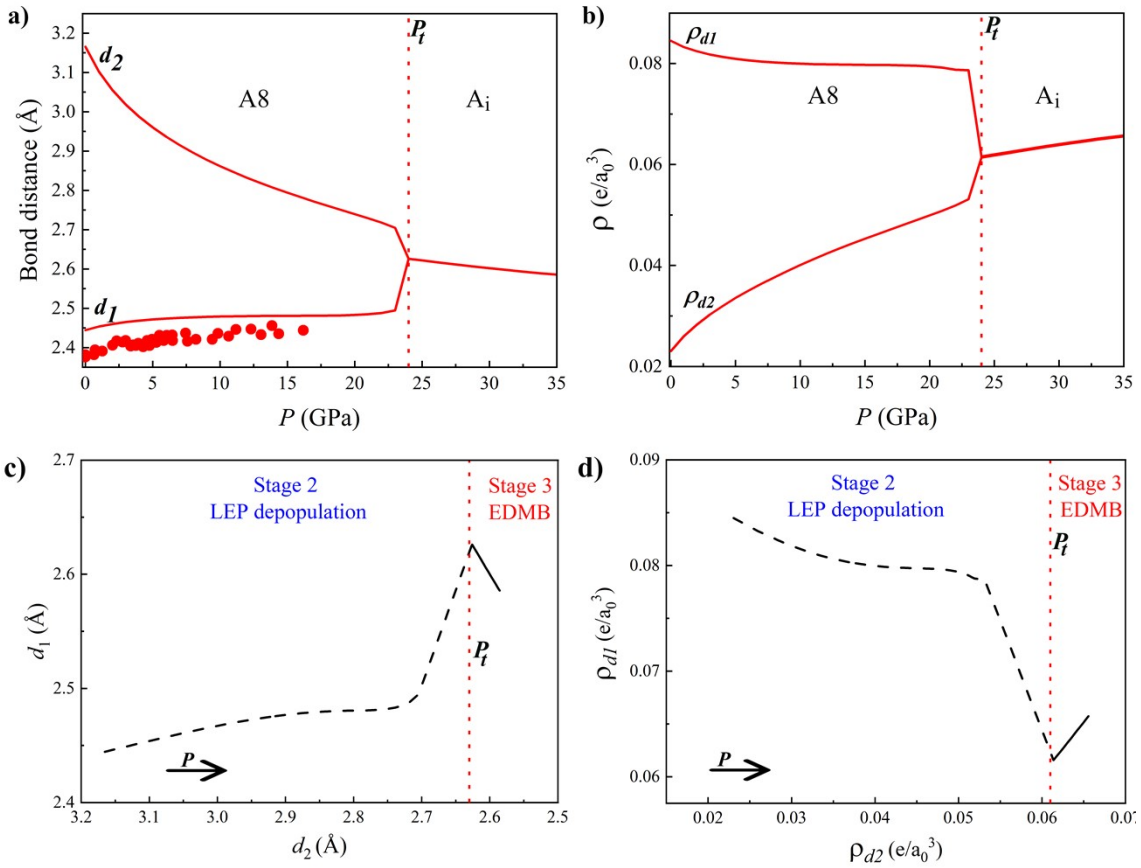


**Figure S8.** Calculated parameters of Se-I as a function of pressure. a) Primary and secondary bond distances, $d_1$ and $d_2$, in the A8 phase of Se. Experimental primary covalent distances (circles) were obtained from Ref. [66]. b) Charge density at the BCP of $d_1$ and $d_2$, $\rho_{d1}$ and $\rho_{d2}$, where $e$ is the electron charge and $a_0$ is the Bohr radius. c) Behavior of $d_1$ vs. $d_2$ and d) the corresponding $\rho_{d1}$ vs. $\rho_{d2}$. The two stages (LEP depopulation and EDMB formation/LEP delocalization) are separated by a vertical red dotted line.

In the case of trigonal Te (Te-I), the atomic volume decreases gradually with pressure as shown in **Fig. S9a**. The evolution of lattice parameters of the Te-I phase with pressure is also shown in **Fig. S9b**. In the pressure range up to 7.2 GPa, a contraction of the *a*-axis is observed, while the *c*-axis shows a slight increase. The ECoN of Te goes up to six at $P_t$ (**Fig. S9c**). A similar drop in both $A_1$ and $E'$ modes is obtained up to 7.2 GPa, where they merge to one mode (see **Fig. S9d**). As previously commented for Se, the lack of agreement of theoretical and experimental phonon modes near $P_t$ is likely due to the lack of anharmonic interactions in calculations (see main text). The pronounced change in the slope of phonon frequencies near $P_t$ is reflected in the pronounced increase of $|\gamma_i|$ at $P_t$ (see inset of **Fig. S9e**). The electron-deficient multicenter character of the bond beyond 7.2 GPa is evidenced by the high values of the calculated average of the diagonal tensor Z* of Te atoms in the A8 and $A_i$ phases (**Fig. S9e**) and of the absolute Grüneisen parameter of the $A_1$ mode in Se (inset of **Fig. S9e**) near $P_t$. The EDMB formation is also evidenced by the evolution of the Laplacian of the charge density in **Fig. S9f**. The calculated pressure dependence of the bond distances and charge densities at the BCPs in A8 and $A_i$ phases of Te are plotted in **Fig. S10**.

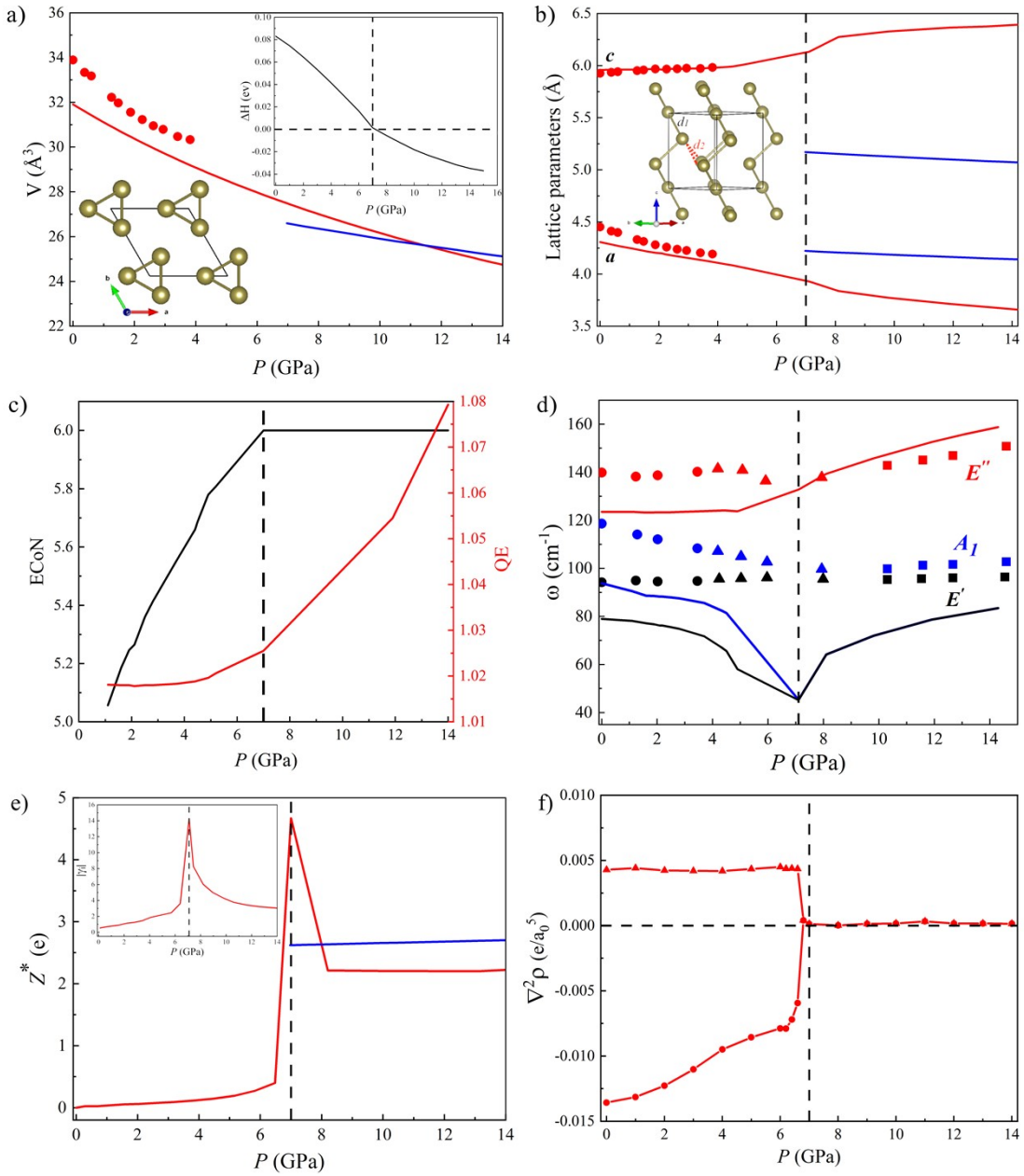


**Figure S9.** Calculated (line) and experimental (symbol) structural parameters of the A8 (red) and $A_i$ (blue) phases of Te under pressure. a) Atomic volume fitted to the BM3-EOS. The attached insets for the ΔH (relative to the $A_i$ phase) and crystal lattice view along the *c*-axis. b) Lattice parameters. An inset of the crystal lattice is attached. Experimental structural data were extracted from Ref. [56]. c) The ECoN (black) and QE (red) of the A8 phase. d) Phonon frequencies, ω, of the A8 phase the $A_1$ mode along the *ab* plane and *E* modes with two double degenerate *E'* and asymmetric stretching *E''* modes. Experimental data points for Te-I (circle), Te-II (triangle), and Te-III (square) were obtained from Ref. [64]. e) Calculated average Born effective charge tensor, Z*, and attached an inset of $|\gamma_i|$ of the $A_1$ mode. f) $\nabla^2\rho$ at the BCP of the primary (circle) and secondary (triangle) bonds of the A8 phase, where e is the electron charge and $a_0$ is the Bohr radius. $P_t$ is marked with vertical dashed lines in all panels.

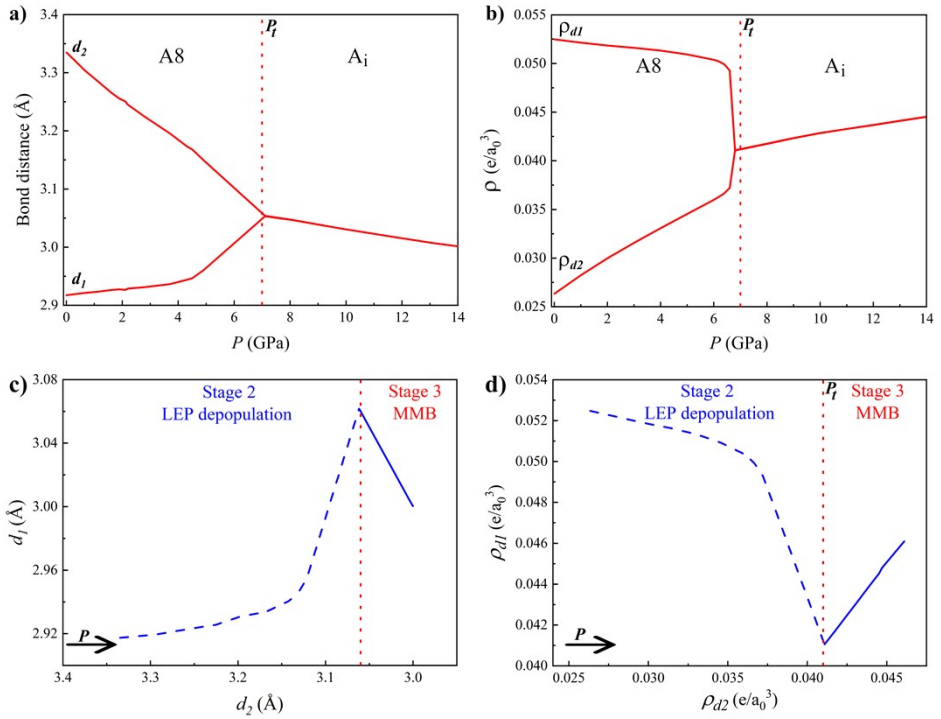


**Figure S10.** Calculated parameters of Te-I as a function of pressure. a) Primary and secondary bond distances, $d_1$ and $d_2$. b) Charge density at the BCP of $d_1$, $\rho_{d1}$, and $d_2$, $\rho_{d2}$. c) Evolution of $d_1$ vs. $d_2$ and d) the corresponding $\rho_{d1}$ vs. $\rho_{d2}$. The two stages (LEP depopulation and EDMB formation/LEP delocalization) are separated by a vertical red dotted line. *e* is the electron charge and $a_0$ is the Bohr radius.

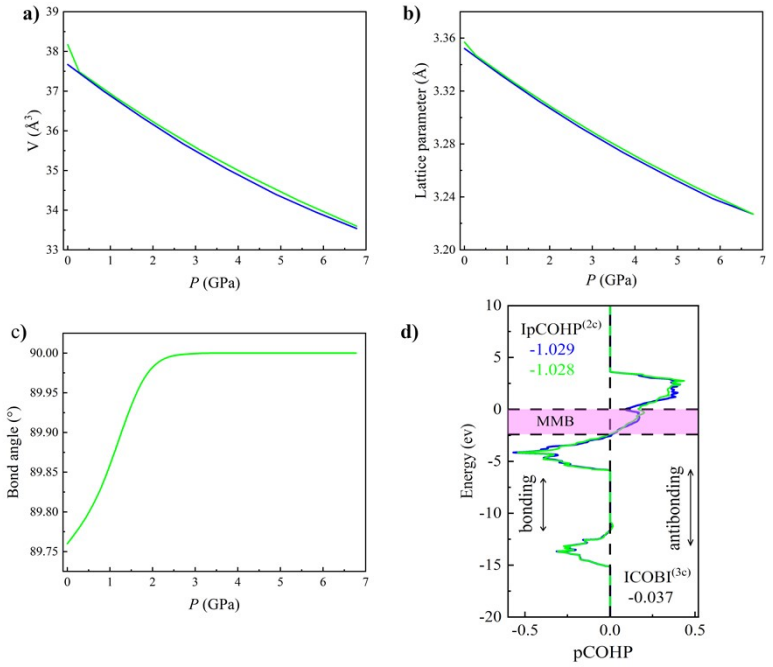


**Figure S11.** Calculated structural parameters for α-Po ($A_h$, solid blue line) and β-Po ($A_i$, solid green line) under hydrostatic pressure. a) Atomic volume, b) lattice parameters, and c) bond angle in the β-Po phase. d) The projected crystal-orbital Hamilton populations (pCOHPs) for the two phases at RP. The shaded region in the pCOHP panel illustrates the antibonding interaction region below the Fermi level characteristic of EDMB formation.

## 5. ELF results of group-15 and -16 elements.

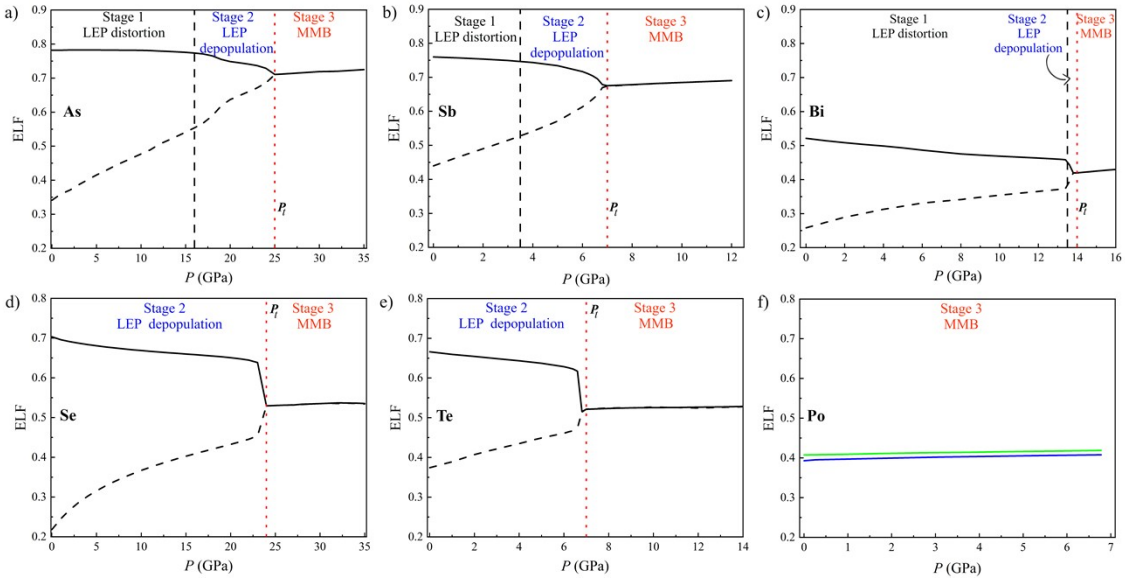


**Figure S12.** Calculated ELF at the bond critical point (BCP) of the primary covalent bond (solid line) and the secondary bond (dashed line) for a-c) group-15 elements (As, Sb, Bi) and d-f) group-16 elements (Se, Te, Po). ELF for the only bond distance in α-Po (blue line) and in β-Po (green line). Vertical black dashed and red dotted lines define the different stages of the mechanism of EDMB formation in group-15 and -16 elements.

## 6. Crystal orbital-based analysis of As under pressure.

**Figure S13** shows the electronic density of states (DOS), the projected crystal-orbital Hamiltonian population (pCOHP), and the crystal-orbital bond index (COBI) calculated for As-I at RP and at HP as well as for As-II at HP. The electronic band structure of As-I at 0 GPa has been already discussed in the literature [67–69]. At 0 GPa, the Fermi level is located in a deep well of the DOS between the bonding (negative COHP and positive COBI values) and antibonding *p*-orbitals (positive COHP and negative COBI values), which is consistent with the semi-metallic character of group-15 elements. Bands below the Fermi level show small antibonding intralayer and interlayer interactions up to -2.5 eV, large bonding intralayer interactions between 2.5 and 7 eV (covalent *ppσ*-bonds), and isolated bonding *s*-type LEPs below 7 eV. It is normally expected to have also states with non-bonding character (near-zero COHP values) near the Fermi level separating bonding and antibonding contributions [70–72]; however, the bands with antibonding character observed just below the Fermi level are characteristic either of the LEP interaction with antibonding orbitals of covalent bonds giving rise to secondary bonds (below 25 GPa in As) or of the formation of EDMBs (above 25 GPa in As) [73].

At 35 GPa, the DOS at the Fermi level is higher than at 0 GPa, so the pseudo-gap separating bonding and antibonding p states are no longer a deep well [74]. Note that calculations for the As-I (A7) and As-II ($A_h$) phases at 35 GPa show similar profiles, being the difference due to a

slight distortion still present in the A7 phase that still results in two bond distances. Tracking the bond strength of primary and secondary As-As interactions with pressure can be achieved by monitoring the values of IpCOHP and ICOBI. IpCOHP represents the overlapping strength along the bonding path, while ICOBI shows the bond order. As pressure increases, both IpCOHP and

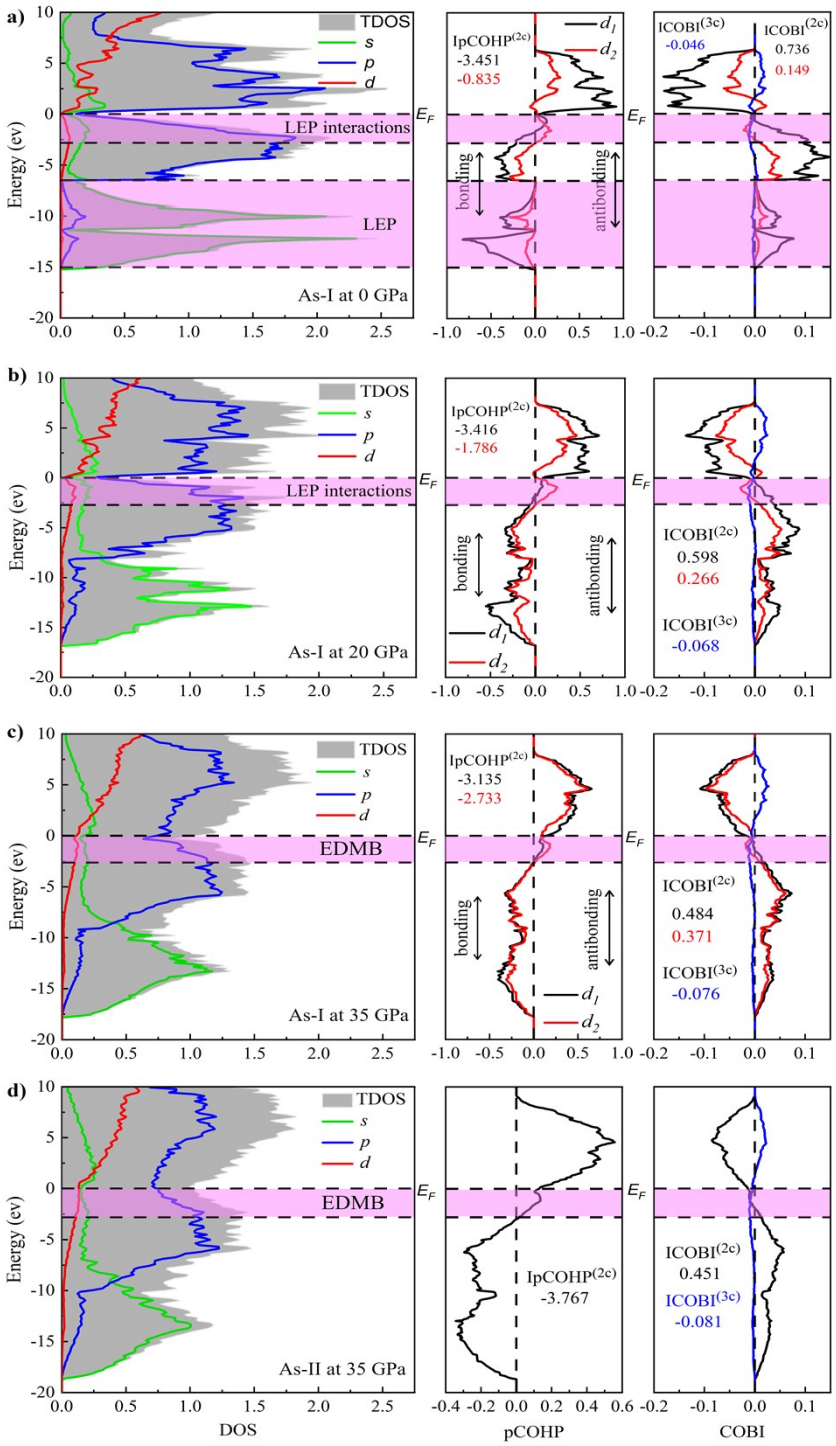


ICOBI monotonically increase, as illustrated in **Fig. S13**.

**Figure S13.** Calculated total and orbital-projected density of states (left), projected crystal-orbital Hamilton population (pCOHP) (center), and crystal-orbital bond index (COBI) (right) for the A7 structure of As at a) 0, b) 20, c) 35 GPa, and d) in $A_h$ phase at 35 GPa. The colored regions illustrate the LEP and its

interactions and also of interactions related to EDMBs. Values for the integrated pCOHP and integrated COBI for two- and three-center interactions are also attached.

## References


[1] G. Kresse, J. Furthmüller, Phys. Rev. B 54 (1996) 11169–11186.

[2] G. Kresse, J. Furthmüller, Comput. Mater. Sci. 6 (1996) 15–50.

[3] G. Kresse, D. Joubert, Phys. Rev. B 59 (1999) 1758–1775.

[4] J.P. Perdew, K. Burke, M. Ernzerhof, Phys. Rev. Lett. 77 (1996) 3865–3868.

[5] P.E. Blöchl, Phys Rev B 50 (1994) 17953–17979.

[6] J.P. Perdew, A. Ruzsinszky, G.I. Csonka, O.A. Vydrov, G.E. Scuseria, L.A. Constantin, X. Zhou, K. Burke, Phys. Rev. Lett. 100 (2008) 136406.

[7] R. Armiento, A.E. Mattsson, Phys. Rev. B 72 (2005) 85108.

[8] A.E. Mattsson, R. Armiento, J. Paier, G. Kresse, J.M. Wills, T.R. Mattsson, J. Chem. Phys. 128 (2008) 84714.

[9] A.E. Mattsson, R. Armiento, Phys. Rev. B 79 (2009) 155101.

[10] H.J. Monkhorst, J.D. Pack, Phys Rev B 13 (1976) 5188–5192.

[11] A. Togo, I. Tanaka, Scr. Mater. 108 (2015) 1–5.

[12] K. Momma, F. Izumi, J. Appl. Cryst. 44 (2011) 1272–1276.

[13] J. Gonzalez-Platas, M. Alvaro, F. Nestola, R. Angel, J. Appl. Crystallogr. 49 (2016) 1377–1382.

[14] A. Otero-de-la-Roza, Á. Martín Pendás, E.R. Johnson, J. Chem. Theory Comput. 14 (2018) 4699–4710.

[15] P. Giannozzi, O. Andreussi, T. Brumme, O. Bunau, M. Buongiorno Nardelli, M. Calandra, R. Car, C. Cavazzoni, D. Ceresoli, M. Cococcioni, N. Colonna, I. Carnimeo, A. Dal Corso, S. de Gironcoli, P. Delugas, R.A. DiStasio, A. Ferretti, A. Floris, G. Fratesi, G. Fugallo, R. Gebauer, U. Gerstmann, F. Giustino, T. Gorni, J. Jia, M. Kawamura, H.-Y. Ko, A. Kokalj, E. Küçükbenli, M. Lazzeri, M. Marsili, N. Marzari, F. Mauri, N.L. Nguyen, H.-V. Nguyen, A. Otero-de-la-Roza, L. Paulatto, S. Poncé, D. Rocca, R. Sabatini, B. Santra, M. Schlipf, A.P. Seitsonen, A. Smogunov, I. Timrov, T. Thonhauser, P. Umari, N. Vast, X. Wu, S. Baroni, J. Phys.: Condens. Matter 29 (2017) 465901.

[16] A.A. Mostofi, J.R. Yates, Y.-S. Lee, I. Souza, D. Vanderbilt, N. Marzari, Comput. Phys. Commun. 178 (2008) 685–699.

[17] A. Otero-de-la-Roza, E.R. Johnson, V. Luaña, Comput. Phys. Commun. 185 (2014) 1007–1018.

[18] A. Dal Corso, Comput. Mater. Sci. 95 (2014) 337–350.

[19] R. Dronskowski, P.E. Bloechl, J. Phys. Chem. 97 (1993) 8617–8624.

[20] V.L. Deringer, A.L. Tchougréeff, R. Dronskowski, J. Phys. Chem. A 115 (2011) 5461–5466.

[21] S. Maintz, V.L. Deringer, A.L. Tchougréeff, R. Dronskowski, J. Comput. Chem. 34 (2013) 2557–2567.

[22] S. Maintz, V.L. Deringer, A.L. Tchougréeff, R. Dronskowski, J. Comput. Chem. 37 (2016) 1030–1035.

[23] J. Donohue, The Structures of the Elements, John Wiley & Sons Ltd., New York, 1975.

[24] H.J. Beister, K. Strössner, K. Syassen, Phys. Rev. B 41 (1990) 5535–5543.

[25] U. Schwarz, L. Akselrud, H. Rosner, A. Ormeci, Yu. Grin, M. Hanfland, Phys. Rev. B 67 (2003) 214101.

[26] O. Degtyareva, M.I. McMahon, R.J. Nelmes, High Press. Res. 24 (2004) 319–356.

[27] O. Degtyareva, M.I. McMahon, R.J. Nelmes, Phys. Rev. B 70 (2004) 184119.

[28] K. Aoki, S. Fujiwara, M. Kusakabe, Solid State Commun. 45, (1983) 161–163.

[29] L.F. Vereshchagin, S.S. Kabalkina, Sov. Phys. JETP 20 (1965) 274.

[30] D. Akhtar, V.D. Vankar, K.L. Goel T. C. and Chopra, J. Mater. Sci. 14 (1979) 988–994.

[31] A.L. Coleman, M. Stevenson, M.I. McMahon, S.G. Macleod, Phys. Rev. B 97 (2018) 144107.

[32] A. Katsutoshi, F. Shuzo, K. Masao, J. Phys. Soc. Japan 51 (1982) 3826–3830.

[33] R.M. Brugger, R.B. Bennion, T.G. Worlton, Phys. Lett. A 24 (1967) 714–717.

[34] L.G. Akselrud, M. Hanflandm, U. Schwarz, Z. Kristallog. - New Cryst. Struct. 218 (2003) 447–448.

[35] I.C. Getting, Metrologia 35 (1998) 119–132.

[36] M.I. McMahon, R.J. Nelmes, Chem Soc Rev 35 (2006) 943.

[37] J.H. Chen, H. Iwasaki, T. Ktkegawa, High Press. Res. 15 (1996) 143–158.

[38] M.I. McMahon, O. Degtyareva, R.J. Nelmes, Phys. Rev. Lett. 85 (2000) 4896–4899.

[39] P. Schaufelberger, H. Merx, M. Contre, High Temp. Pressure 5 (1973) 221–230.

[40] Y. Akahama, H. Kawamura, A.K. Singh, J. Appl. Phys. 92 (2002) 5892–5897.

[41] B. Cordero, V. Gómez, A.E. Platero-Prats, M. Revés, J. Echeverría, E. Cremades, F. Barragán, S. Alvarez, Dalton Trans. (2008) 2832–2838.

[42] G. Parthasarathy, W.B. Holzapfel, Phys. Rev. B 38 (1988) 10105–10108.

[43] O. Degtyareva, E. Gregoryanz, H.K. Mao, R.J. Hemley, High Press. Res. 25 (2005) 17–33.

[44] C. Hejny, M.I. McMahon, Phys. Rev. Lett. 91 (2003) 215502.

[45] P.W. Bridgman, Phys. Rev. 48 (1935) 893–906.

[46] P.W. Bridgman, Phys. Rev. 60 (1941) 351–354.

[47] J.C. Jamieson, D.B. McWhan, J. Chem. Phys. 43 (1965) 1149–1152.

[48] A. Katsutoshi, S. Osamu, M. Shigeru, J. Phys. Soc. Japan 48 (1980) 551–556.

[49] G. Parthasarathy, W.B. Holzapfel, Phys. Rev. B 37 (1988) 8499–8501.

[50] R.J. DeSando, R.C. Lange, J. Inorg. Nucl. Chem. 28 (1966) 1837–1846.

[51] W. Hume-Rothery, G. V Raynor, The Structure of Metals and Alloys, 3^rd, Institute of Metals Monograph and Report Series, London, 1954.

[52] A. von Hippel, J. Chem. Phys. 16 (1948) 372–380.

[53] D. Schiferl, C.S. Barrett, J. Appl. Cryst. 2 (1969) 30–36.

[54] C.S. Barrett, P. Cucka, K. Haefner, Acta Cryst. 16 (1963) 451–453.

[55] P. Cucka, C.S. Barrett, Acta Cryst. 15 (1962) 865–872.

[56] R. Keller, W.B. Holzapfel, H. Schulz, Phys. Rev. B 16 (1977) 4404–4412.

[57] L.F. Mattheiss, D.R. Hamann, W. Weber, Phys. Rev. B 34 (1986) 2190–2198.

[58] N.G. Pace, G.A. Saunders, Z. Sümengen, J. Phys. Chem. Solids 31 (1970) 1467–1476.

[59] K. Takumi, I. Hiroshi, J. Phys. Soc. Japan 56 (1987) 3417–3420.

[60] M. Wuttig, V.L. Deringer, X. Gonze, C. Bichara, J.-Y. Raty, Adv. Mater. 30 (2018) 1803777.

[61] D. Schiferl, D.T. Cromer, J.C. Jamieson, Acta. Cryst. B 37 (1981) 807–810.

[62] X. Wang, K. Kunc, I. Loa, U. Schwarz, K. Syassen, Phys. Rev. B 74 (2006) 134305.

[63] Y. Zhao, S. Clément, J. Haines, R. Viennois, J. Phys. Chem. C. 124 (2020) 26659–26669.

[64] H. Olijnyk, S. Nakano, K. Takemura, Phys. Status Solidi B 244 (2007) 3572–3582.

[65] X. Li, X. Huang, X. Wang, M. Liu, G. Wu, Y. Huang, X. He, F. Li, Q. Zhou, B. Liu, T. Cui, Phys. Chem. Chem. Phys. 20 (2018) 6116–6120.

[66] T. Masaharu, N. Kiyofumi, J. Phys. Soc. Japan 76 (2007) 17–18.

[67] M.H. Cohen, L.M. Falicov, S. Golin, IBM J. Res. Dev. 8 (1964) 215–227.

[68] X. Gonze, J.-P. Michenaud, J.-P. Vigneron, Phys. Rev. B 41 (1990) 11827–11836.

[69] P.K. Silas, P.D. Haynes, J.R. Yates, Phys. Rev. B 88 (2013) 134103.

[70] U. V Waghmare, N.A. Spaldin, H.C. Kandpal, R. Seshadri, Phys. Rev. B 67 (2003) 125111.

[71] M. Wuttig, D. Lüsebrink, W. Wamwangi Daniel and Wełnic, M. Gilleßen, R. Dronskowski, Nat. Mater. 6 (2007) 122–128.

[72] T.H. Lee, S.R. Elliott, Adv. Mater. 29 (2017) 1700814.

[73] T.H. Lee, S.R. Elliott, Nat. Commun. 13 (2022) 1458.

[74] U. Häussermann, K. Söderberg, R. Norrestam, J. Am. Chem. Soc. 124 (2002) 15359–15367.